

See discussions, stats, and author profiles for this publication at: <https://www.researchgate.net/publication/231230910>

# Synthesis of Monodisperse Magnetic Iron Oxide Nanoparticles from Submicrometer Hematite Powders

ARTICLE *in* CRYSTAL GROWTH & DESIGN · FEBRUARY 2008

Impact Factor: 4.89 · DOI: 10.1021/cg0706013

---

CITATIONS

23

---

READS

27

7 AUTHORS, INCLUDING:



**Chun-Rong Lin**

Southern Taiwan University of Science and...

56 PUBLICATIONS 523 CITATIONS

SEE PROFILE



**I. S. Lyubutin**

Russian Academy of Sciences

282 PUBLICATIONS 1,128 CITATIONS

SEE PROFILE



**Hsin-Yi Lai**

National Cheng Kung University

28 PUBLICATIONS 342 CITATIONS

SEE PROFILE

# Synthesis of Monodisperse Magnetic Iron Oxide Nanoparticles from Submicrometer Hematite Powders

Chih-Jung Cheng,<sup>†,\*</sup> Chee-Cheng Lin,<sup>†</sup> Ray-Kuang Chiang,<sup>\*,†</sup> Chun-Rong Lin,<sup>§</sup>  
Igor S. Lyubutin,<sup>\*,‡</sup> Egor A. Alkaev,<sup>‡</sup> and Hsin-Yi Lai<sup>‡</sup>

*Nanomaterials Laboratory, Far East University, Hsing-Shih, Tainan County 74448, Taiwan,  
Department of Mechanical Engineering, National Cheng Kung University, Tainan 701, Taiwan,  
Department of Mechanical Engineering, Southern Taiwan University of Technology, Tainan County  
710, Taiwan, and Institute of Crystallography, Russian Academy of Sciences, Moscow 119333, Russia*

Received June 30, 2007; Revised Manuscript Received October 3, 2007

**ABSTRACT:** This study identifies submicrometer hematite ( $\alpha$ -Fe<sub>2</sub>O<sub>3</sub>) powder as a cost-effective and efficient starting material for the synthesis of monodisperse magnetic iron oxide nanoparticles (MMIONPs). The feature of this process is the slow dissolution of hematite powder in a mixture of unsaturated fatty acids and organic solvents. The hematite particles are dissolved by the complexation of their iron with the unsaturated fatty acid ligands to give iron acid salt as a soluble compound. This method presents an interesting example for the production of monodisperse oxide NPs from bulk oxide powder with a moderate solubility in fatty acids. Conceptually, it can be simply viewed as a controlled dissolution–recrystallization process. The relatively low solubility of magnetic iron oxides (maghemite and magnetite) in the reaction condition determines their appearance in the recrystallization process. Moreover, the monodispersity of the formed NPs is sustained during the whole process, which results from the slow supply and the fast consumption of growing units by the slow dissolution of hematite and the fast enough growth rate of magnetic iron oxide NPs. The compositions of the MMIONPs were determined by Mössbauer spectroscopy. It appears that  $\gamma$ -Fe<sub>2</sub>O<sub>3</sub> is preferentially precipitated out at lower ligand concentrations, while the Fe<sub>3</sub>O<sub>4</sub> appears along with  $\gamma$ -Fe<sub>2</sub>O<sub>3</sub> at higher ligand concentrations.

## Introduction

Monodisperse nanoparticles (NPs) of various materials are essential in the precise determination of their size-dependent properties in the nanoscale range.<sup>1</sup> Moreover, the fast growing interest in ordered nanomaterials for novel applications via the self-assembly of monodisperse NPs further stresses their role as building units in the construction of nanostructured materials.<sup>2</sup> Thus, facile and economical methods for easily repeatable products of monodisperse NPs of various materials are of crucial importance to the development of nanotechnology. NPs find applications in many branches of science and engineering depending upon the nature of the NPs and their assembly patterns. For example, magnetic iron oxide (maghemite or magnetite) NPs find applications in areas such as separation of pollutants, carriers for drug targeting, hyperthermia treatment of cancer cells, magnetic storage, metamaterials, etc. New synthetic methods have been flourishing for the control of their sizes, size uniformity, and shapes. Among the many reported methods, thermal decomposition of a soluble iron precursor in a mixture of surfactant and high bp organic solvent is the method most frequently used, which leads to well-controlled products of monodisperse magnetic iron oxide nanoparticles (MMIONPs). Iron-containing precursors such as Fe(CO)<sub>5</sub>,<sup>3</sup> Fe(Cup)<sub>3</sub>,<sup>4</sup> Fe(acac)<sub>3</sub>,<sup>5</sup> Fe(acac)<sub>2</sub>,<sup>6</sup> iron carboxylates (including formates, acetates, and long-chain carboxylates),<sup>6,7</sup> iron organometallic compounds,<sup>8</sup> and amorphous iron oxyhydroxides<sup>9</sup> have been used as starting materials in the syntheses, as long as they are soluble in the reaction system. In general, a very soluble precursor is preferred for the synthesis of MMIONPs. This is

probably because their precipitation from a homogeneous system is conceptually easy to handle. It is also easy to meet the primary rule for the synthesis of a monodisperse system: a distinct separation between the nucleation stage and the growth stage.<sup>10</sup> As a result, materials with poor solubility in the reaction system generally receive much less attention upon preparing MMIONPs by solvent-media thermal decomposition methods.

The reported methods on the synthesis of magnetic iron oxide nanoparticles based on oxide precursor are somewhat obscure. Peng et al. described that transition metal oxide NPs from a process using oxide powder precursors that worked in some cases but was not as repeatable as the process using metal soap precursors.<sup>7a</sup> As a result, they did not give any experimental details on the oxide-precursor process in their study. On the other hand, Yu et al. have tried using commercially available iron oxides as precursors in the synthesis of Fe<sub>3</sub>O<sub>4</sub> NPs by thermolysis.<sup>9</sup> However, their successful examples were limited to a fully dissolved precursor, 2-line ferrihydrite. These and other studies have all proven that the metal fatty acid salts are the intermediate precursors for the organic-phase preparation of monodisperse oxide NPs in the presence of long-chain carboxylic acids, although the detailed mechanism to the well-controlled monodisperse system is not clear. Thus, the transformation of bulk oxide powder to long-chain carboxylate salts of metals, metal soaps, should be the key step in the successful synthesis of oxide NPs using bulk oxide starting materials.

Clues derived from the known process for the preparation of metal soaps<sup>11</sup> suggest that some oxides are very soluble in hot long-chain carboxylic acids to give metal soaps, which can be used as precursors to prepare NPs.<sup>12</sup> For example, zinc stearate can be prepared from bulk ZnO powder and stearic acid by fusion methods.<sup>13</sup> It is thus not surprising to find that bulk zinc oxide powder has been used as the precursor to prepare the ZnO NPs in a one-pot process.<sup>14</sup> Conceptually, if the bulk metal oxide is very soluble in a long-chain fatty acid, the formation of NPs from the soluble system can be recognized as a controlled

\* Correspondence should be addressed to rkc.chem@msa.hinet.net (R.-K.C., synthesis and characterization) and/or lyubutin@ns.crys.ras.ru (I.S.L., Mössbauer spectroscopy).

<sup>†</sup> Far East University.

<sup>‡</sup> National Cheng Kung University.

<sup>§</sup> Southern Taiwan University of Technology.

<sup>‡</sup> Russian Academy of Science.

dissolution–recrystallization process and the acid can be viewed as the solvent.<sup>15</sup> Thermodynamically, a soluble oxide implies its low stability in the solvent system.<sup>16</sup> Indeed, a soluble oxide precursor does not ensure the nucleation and frequently suffers from long incubation time for nucleation.<sup>17</sup> Thus, an activator is frequently necessary to promote the nucleation and growth. As indicated by Peng et al., adding octylalcohol which reacted with stearate ligands in the synthesis of ZnO NPs promoted the nucleation.<sup>18</sup> However, in the reported synthesis of MMIONPs via the long-chain carboxylate precursors, there are generally no activators required. Thermodynamically, the least soluble (the most thermodynamically stable) oxide should be the final product for metal oxides containing many different forms, if we consider the protecting factors on the interfaces of various iron oxides to be similar. In other words, the type of iron oxide that does not show up in the product could be the more soluble phase in the reaction conditions. Following this thought, we have tried various types of iron oxides other than the magnetic iron oxide as starting materials for the synthesis of MMIONPs. In this paper, we reported the dissolution behavior of hematite in unsaturated fatty acids and its application to the synthesis of MMIONPs.

### Experimental Section

**Chemicals.** Hematites ( $\alpha\text{-Fe}_2\text{O}_3$ ) were obtained from J. T. Baker, Aldrich, Acros, and Showa Chemicals. Oleic acid (OA, 90%, Showa), 1-octadecene (ODE, 90%, Acros), linoleic acid (60%, Acros), ricinoleic acid (80%, TCI), and 1-eicosene (99%, TCI) were used as received without further purification.

**Syntheses of Iron Oxide NPs in Hot Fatty Acids.** In a typical reaction, a mixture of bulk  $\alpha\text{-Fe}_2\text{O}_3$  powder (3 mmol) and oleic acid (26 mmol, 9.0 mL) was loaded in a three-necked round-bottom flask and was then heated to 320 °C ( $\sim 15$  °C/min). The temperature is controlled by a heating mantle and thermocouple above a magnetic stirrer. During the reaction, the mixture bubbled and spilt seriously because of the generation of water. This can be reduced by distilling out the generated water. The color of the reactant changed from red to brown to black during the reaction. The resulting products were diluted with hexane and centrifuged at speed of 5000 rpm. The residues of the centrifuge were washed with ethanol, dried, and weighed. The supernatant was precipitated with copious amount of acetone, and the precipitate was washed with acetone and ethanol two or three times. The phase of the precipitate was checked by X-ray diffraction (XRD). The thermogravimetric measurements were used to determine the amount of solid oxide in the dried samples. The precipitated NPs can be redispersed in hexane. The transmission electron microscopy (TEM) samples were prepared by dropping the hexane suspension onto a copper grid (200 mesh) coated with carbon film. The size of each NP was determined by averaging the major and the minor axes using a Sigmascan Pro 5. The standard deviation of the size distribution of the NPs was calculated based on more than 500 particles in the TEM micrograph.

**Synthesis of Monodisperse Iron Oxide NPs.** The high-boiling-point solvent used is mainly ODE, which is a proper solvent used in the synthesis of quantum dots and iron oxide NPs. The reaction parameters used in the synthesis of a series of MMIONPs are listed in Table 1. In a typical reaction, a mixture of  $\alpha\text{-Fe}_2\text{O}_3$ , oleic acid, and 1-octadecene is heated to a temperature in the range of 300 to 340 °C in a round-bottom flask fitted with a condenser under a flow of argon. The workup procedures are similar to that described in the previous section.

**Structure and Phase Evolution Studies.** For studying the evolution of the reactions, samples were collected from the reaction mixture at an interval of 30 min. Drops of sample were extracted from reaction bottles for Fourier transform infrared (FTIR) and TEM measurements. Samples required in large amounts for measurements such as XRD were prepared in separated runs stopped at the specified reaction time by moving the flask from the heating element and cooling in air. The samples were collected by precipitation with acetone and centrifuged at speeds of 5000 rpm.

**Table 1. Synthesis of MMIONPs with Different Sizes from Hematite Powders Showing the Reaction Composition, Temperature, and Time**

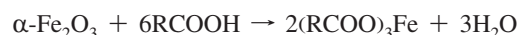
run	hematite (mmol)	acid <sup>a</sup> (mL)	solvent <sup>b</sup> (mL)	temp (°C)	time (h)	diameter (nm)
1	1.5	9	18	320	3.5	8.8 ± 0.4
2	3	6	12	320	3.5	10.6 ± 0.6
3	3	9	18	320	4	12.1 ± 0.5
4	3	9	18	320	4	14.5 ± 0.8
5	3	12	18	320	4.5	18.1 ± 1.8
6	3	9	18	320	4	19.2 ± 2.3
7	3	12	18	340	6	22.3 ± 3.5

<sup>a</sup> Acids used: run 1–3, oleic acid; run 4–6, linoleic acid; run 7, ricinoleic acid. <sup>b</sup> Solvent used: run 1–6, 1-octadecene; run 7, 1-eicosene.

**Instrumentation.** The phases of the products were characterized by X-ray powder diffraction (Shimadzu XRD-6000) using Cu K $\alpha$  radiation. The transmission electron microscope (JEOL JEM 1200EX) with an accelerating voltage of 80 kV and the high-resolution transmission electron microscope (Philips Tecnai G2 F20 or JEOL JEM 2010) with an accelerating voltage of 200 kV were used for the imaging work. Scanning electron microscopy (SEM) micrographs of hematite powder were obtained on a field emission SEM (FE-SEM) instrument (JEOL JSM 7000). The Micromeritics ASAP 2010 was used to determine the specific surface area of the hematite powder by the BET method at 77 K. The Fourier transform infrared spectra (Nicolet 5700) were operated with a resolution of 4 cm<sup>−1</sup>. The content of iron oxide in the dried precipitate was determined by using a thermogravimetric analyzer (TGA) under a constant flow of N<sub>2</sub> gas. Mössbauer studies were performed on a spectrometer equipped with a low temperature setup. The  $\gamma$ -ray source <sup>57</sup>Co(Rh) was at room temperature, and the isomer shifts were measured relative to metal  $\alpha$ -Fe at room temperature.

### Results and Discussion

**Dissolution of Hematite in Oleic Acid.** The dissolution of hematite could be dependent upon factors such as solvent composition, temperature, and quality and the characteristics of the oxide itself. The hematite powders were obtained from several different chemical suppliers for selection of proper candidates. The powders obtained from J. T. Baker with the highest BET surface area of 13.4 m<sup>2</sup>/g were chosen as a precursor in this study. Hematite powders with surface areas in this range can also be obtained from a wet process of neutralization of the pickling waste of the steel industry. The SEM images of the hematite acquired showed that they are secondary particles agglomerated from smaller primary particles with sizes in the range of several hundred nanometers. Below 300 °C, the hematite powders acquired did not show appreciable solubility in the fatty acids after a duration of 3 h. This was manifested by no change of the red color during the process, and no phase change in the FTIR and XRD. However, it was found that the red color of hematite was gradually changed from red to reddish brown as the reaction temperatures were raised above 300 °C after 30 min. The dissolution is also accompanied by violent bubbling and spilling because of the generated water boiling at a high temperature. The FTIR of a 2-h sample from the reaction mixture of hematite and oleic acid at 320 °C showed that a new peak at 1551 cm<sup>−1</sup> was formed, which is consistent with the C–O stretching of the as-formed iron carboxylate bonds that is more constrained than that of the free acids (1709 cm<sup>−1</sup>), Figure 1. The observed phenomena are consistent with the formation of iron oleate and water as in the following idealized formula.



Time-evolved samples of the dissolution reaction were also characterized by TEM, selected area electron diffraction (SEAD),



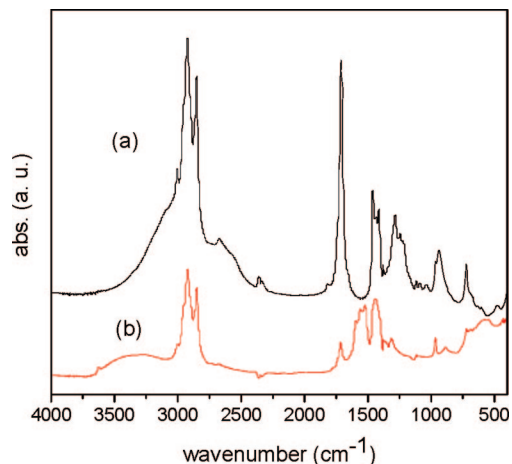


**Figure 1.** FTIR spectra of (a) oleic acid and (b) a 2-h sample from the reaction mixture of the dissolution of hematite in hot oleic acids showing the formation of iron oleates.

and X-ray powder diffraction (XRD), Figures 2 and 3. Aggregates of amorphous particles with sizes of 3–4 nm were observed in the 30- and 60-min samples by TEM. NPs with poor crystalline phase start to form after the 90 min, as shown in Figure 2c. However, the particles of all the three samples only appeared in low concentration as they only showed up scarcely on the TEM grids. The color of the reaction mixture turned to brown after 2 h, and the XRD pattern of the sample appeared as an amorphous phase, Figure 3d, which indicated that the iron oleate became the dominate phase in the reaction mixture. However, we also found NPs in small amounts by TEM with sizes of about 15 nm showing diffraction attributed to spinel structure. This indicated that the magnetic iron oxide NPs have started to form by decomposition of the iron oleate at the same time. Finally, the NPs become the dominant phase in 150- and 180-min samples on the XRD patterns, Figure 3e and f. On the other hand, as indicated in TEM, the shape of the NP became more spherelike by Ostwald's ripening process and finally gave NPs with sizes of  $15.7 \pm 2.3$  nm. On the basis of the above evidence, submicrometer hematite powders are soluble in hot oleic acid and give the iron oleates as products, which are further decomposed to magnetic iron oxide NPs. However, the monodisperse system is not reached. Possibly, the as-formed NPs are also soluble in this high ligand concentration condition. As a result, the intermediate high monomer concentration led to the second nucleation and the polydisperse system.

**Dissolution of Hematite in Oleic Acid and ODE.** Since the high ligand concentration is not helpful in the formation of a monodisperse system, we try to dilute the oleic acid with the ODE solvent, Table 1 run 3. In order to understand the structure and phase evolution during the transformation, samples are also collected at an interval of 30 min for a 3-h duration as described in the experimental section. Time-evolved samples were also characterized by TEM and XRD, Figures 4 and 5. Upon dissolution, the surface of the  $\alpha$ -Fe<sub>2</sub>O<sub>3</sub> particles is etched with the formation of amorphous particles of about 4 nm after about 30 min, Figure 4b. Both the NPs and partially dissolved hematite particles are present in the system for the next 2 h. The size of the formed iron oxide NPs increased with reaction time as the dissolution of hematite particles continued. Interestingly, the particles formed at each stage appeared very homogeneous in size. Growth by particle aggregation was not observed. Finally, MMIONPs with sizes of  $12.1 \pm 0.5$  nm were obtained after 4 h. The unreacted residue can be easily separated by centrifuge,

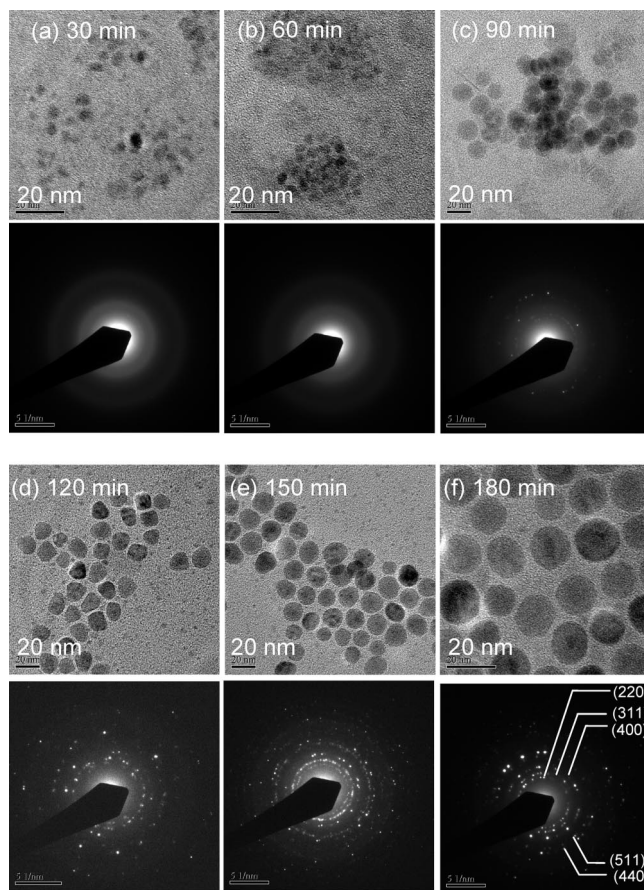


**Figure 2.** Time-evolved samples of the dissolution of submicrometer hematite in oleic acid characterized by TEM and selected area electron diffraction (SEAD) shown in parts a–f (reaction time, average particle sizes): (a) 30 min,  $4.0 \pm 1.0$  nm; (b) 60 min,  $4.4 \pm 0.9$  nm; (c) 90 min,  $14.3 \pm 2.5$  nm; (d) 120 min,  $14.5 \pm 1.5$  nm; (e) 150 min,  $15.3 \pm 1.5$  nm; and (f) 180 min,  $15.7 \pm 2.3$  nm. Aggregates of amorphous particles with sizes of about 4 nm were observed in the 30- and 60-min samples. NPs with poor crystalline phase started to form in the 90-min sample. However, the NPs of the above three samples only appeared in low concentration as they only showed up scarcely on the TEM grids. NPs in small amounts with sizes of about 15 nm in the 120-min sample showed diffraction peaks attributed to the spinel structure. Finally, the NPs become the dominant phase in the 150- and 180-min samples with spherelike shapes by Ostwald's ripening process.

and its amount was only about 5% of the hematite powder loaded. The SEM micrograph and XRD pattern of the residue indicated that it is hematite of large particle sizes. XRD samples at the specified reaction time from separated runs were also carried out to learn more about the relative compositions. The relative peak intensities show a trend that the peaks intensity of MMIONPs increased with the decreased intensity of hematite as time evolved, Figure 5. Crystalline magnetic iron oxide nanoparticles (with reflections arisen from magnetite or maghemite) become detectable after about 90 min. The diffraction peaks of hematite disappeared after 150 min. This is consistent with what was observed in TEM and confirms the slow dissolution of hematite.

**Synthesis of Monodisperse Iron Oxide NPs.** On the basis of the above results, dilution with solvent is beneficial to the synthesis of a monodisperse system, although it slows down the dissolution a little. Thus, a series of runs based on conditions similar to those above, which are a optimal conditions based on the results from many test runs, have been carried out, Table

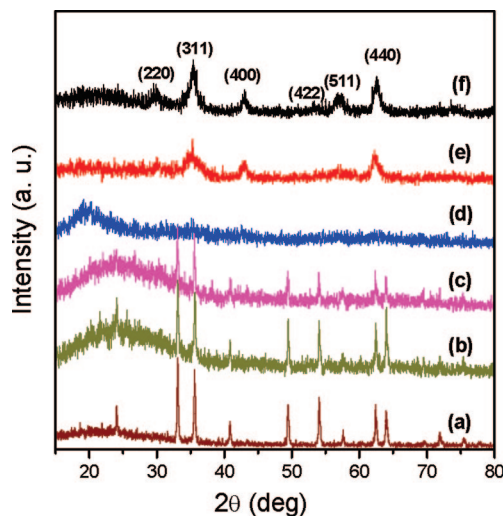


**Figure 3.** XRD powder patterns of intermediate samples of hematite dissolved in hot oleic acids at different reaction times (a) 30, (b) 60, (c) 90, (d) 120, (e) 150, and (f) 180 min showing the phases gradually changing from hematite to spinel oxide.

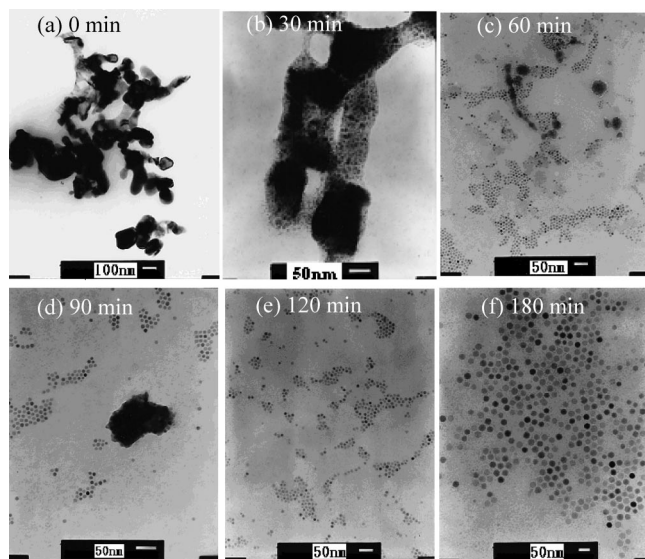


**Figure 4.** (a–f) TEM images of intermediate samples of hematite dissolved in a hot mixture of oleic acids and ODE at different reaction times showing the dissolution of hematite powder, recrystallization of NPs, and the seed-mediated growth to the final monodisperse NPs.

1. The TEM micrographs of the monodisperse samples frequently revealed a close packed pattern because of their highly homogeneous particle sizes, Figure 6. Both the electron diffraction, Figure 6h, and the XRD patterns, Figure 7, indicate that a spinel structure was obtained. Magnetization measurements of all the NPs obtained revealed superparamagnetic behavior at room temperature (see the Supporting Information, Figure S1). The saturation magnetization decreased as the particle size decreased. This phenomenon can be interpreted as the effect of surface spin canting when the particle size is reduced. In this set of experiments, the size of NPs can be tuned by parameters such as the amount of hematite powders loaded, reaction temperature, and concentration of acids. It appeared that other unsaturated fatty acids such as linoic acid and ricinoic acid also worked as well. These unsaturated fatty acids used are with either a different number of double bonds or extra functionality, which lead to the different molecular shapes.

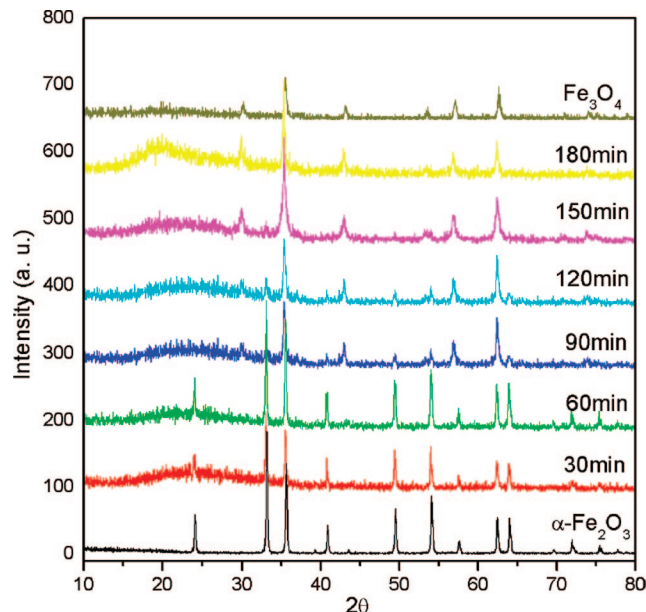


**Figure 5.** The XRD powder patterns of intermediate samples of hematite dissolved in a hot mixture of oleic acids and ODE at different reaction times.

When they are attached on the surfaces of the formed nanoparticles, their coverage on the surfaces of NPs is different. Thus, different dissolution and growth rates may exist, which lead to different sizes of the NPs formed. Results also show a trend that higher reaction temperatures and high ligand concentrations lead to larger particle sizes.

**Factors Affecting the Quality of NPs.** The role of oleic acids is multiple in this reaction, which is a ligand leaching the surface of hematite particles and as-formed NPs, a protecting surfactant for the as-formed NPs, and also the solvent. Its concentration has an effect on the size and size homogeneity of the final product. The size of NPs is larger at higher concentrations of acids, run 4 and run 5 in Table 1. When a high acid concentration is used, the dissolution increased both on the hematite particle and on the as-formed magnetic iron oxide nuclei. Thus, the formation of stable nuclei became harder because larger nuclei are required to survive the redissolution. As a result, the particle size of the stable nuclei (the critical size) is larger at a high concentration of carboxylic acids, and it frequently needs more time to form. The reaction temperature has a similar effect. Also, at a high acid concentration, the second nucleation is not easy to prevent because it is still possible that a high concentration of monomer is present. As a consequence, a monodisperse system is hard to reach for such a high concentration of carboxylic acids. When a lower concentration of acid is used, the dissolution rate of hematite powders is lower and so is the monomer concentration. When the monomer concentration is kept less than the critical concentration of second nucleation, a monodisperse system is thus sustained. In this case, the monomers are consumed by the monomer-addition growth process only. Accordingly, the size homogeneity of NPs obtained is sustained in the whole process.

**Mechanism.** Generally speaking, the size of NPs obtained from the method using hematite precursor is larger than that from a fully soluble precursor, if similar reaction parameters were used. The coexistence of gradually dissolved  $\alpha$ -Fe<sub>2</sub>O<sub>3</sub> particles and gradually grown magnetic iron oxide nanoparticles in the system is responsible for this. The submicrometer hematite



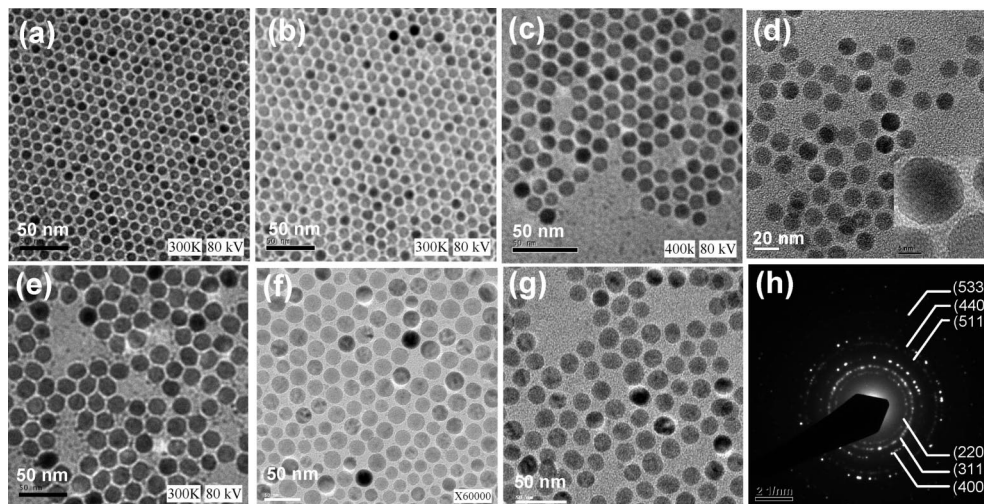


**Figure 6.** TEM micrographs of NPs prepared from hematite powders treated in hot mixtures of oleic acids and organic solvents at 320–340 °C for 3.5–6 h (see Table 1 for details) showing products with homogeneous sizes in the range of 8.8–22.3 nm. The acids used were the following: (a–c) oleic acid; (d–f) linoleic acid; (g) ricinoleic acid. The solvents used were the following: (a–f) 1-octadecene; (g) 1-eicosene; (h) typical select area diffraction from the MMIONPs obtained.

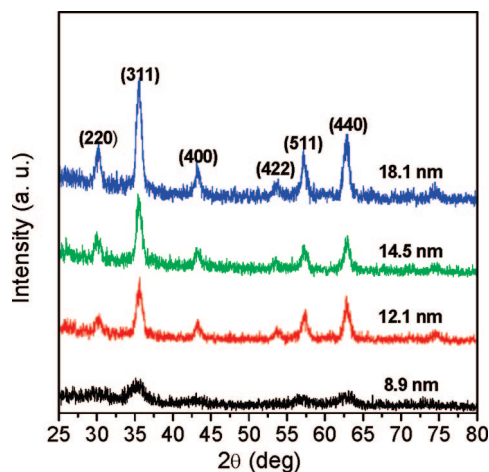


**Figure 7.** X-ray powder diffraction patterns of NPs prepared from hematite powders treated in hot mixtures of oleic acids and organic solvents under the reaction conditions listed in Table 1 showing broadened peaks attributed to the inversed spinel NPs.

particles act as a reservoir of the growing units during the formation of monodisperse nanoparticles, which is different from the process using a fully soluble precursor. The growth in the later stage in this hematite method is a typical seed-mediated growth. As a result, the higher the amount of hematite loaded, the larger the size of NPs obtained; for example, see runs 1 and 3 in Table 1. Moreover, the slow rate of dissolution of hematite at an optimal acid concentration ensures there is no abrupt increase of monomers. On the other hand, the growth rate of NPs is also important, because the final concentration of monomer relies on both the dissolution rate of hematite and the growth rate of MMIONPs. The growth by decomposition of iron-carboxylates appears as a fast step based on the reported data. Thus, the monomer concentration is always low. As a whole, this process provides an interesting example of a controlled dissolution–recrystallization process followed by seed-mediated growth to produce the MMIONPs. The finally formed monodisperse iron oxide nanocrystals sustain for hours at the reaction temperature without changing their size and size uniformity indicating the stability of the formed NPs in contrast

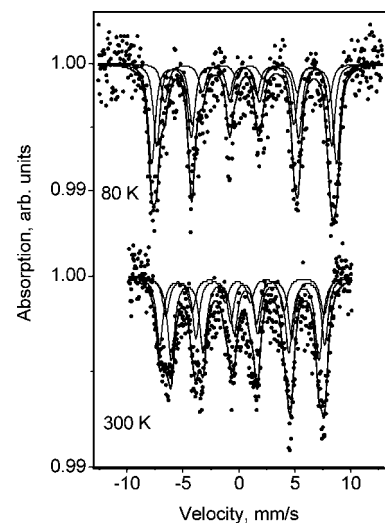


**Figure 8.** Mössbauer spectra of the monodisperse iron oxide NPs with diameters of 18.1 nm (run 5 in Table 1) obtained at 300 and 80 K. Solid lines are least-squares fits of the experiment to superposition of three components with the hyperfine parameters listed in Table 2.

to the soluble hematite precursors in the solvent system at the reaction temperature.

**Mössbauer Spectroscopy.** Mössbauer spectroscopy was also applied in order to learn the phase composition and magnetic properties of the nanoparticles. The  $^{57}\text{Fe}$ -Mössbauer spectra of the monodisperse particles with sizes of 18.1, 12.1, 10.6, and 8.8 nm were recorded at temperatures of 80–300 K in the transmission geometry with a standard spectrometer operating in the constant accelerations regime. We have found that only the particles with a size of 18.1 nm exhibit a well-developed magnetic hyperfine splitting at room temperature, Figure 8, indicating magnetic ordering of Fe ions, Figure 8 and Figure S2. This means that the blocking temperature  $T_b$  (or Neel temperature  $T_N$ ) of these particles is higher than room temperature. It is obvious from the shape of the room-temperature spectra of the 18.1-nm particles that their composition is not a single phase. The spectrum can be fit to three six-line components with hyperfine parameters given in Table 2. From the

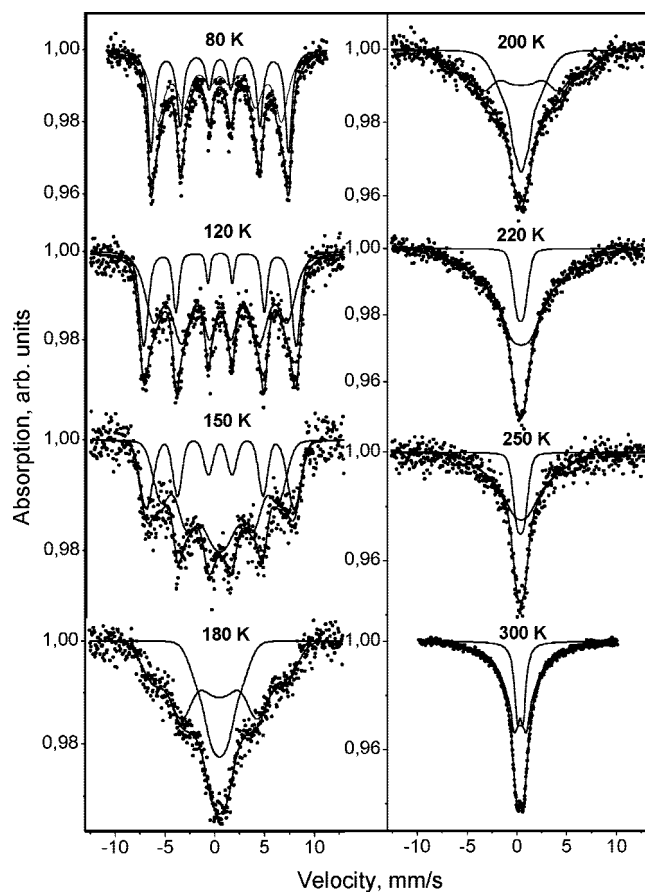
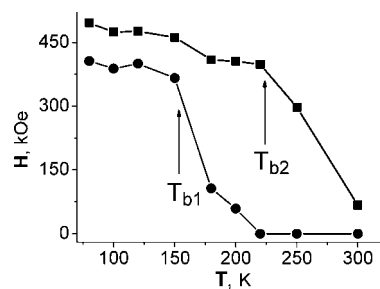
**Table 2.** Hyperfine Parameters of the  $^{57}\text{Fe}$ -Mössbauer Spectra for Monodisperse Nanoparticles of Iron Oxides with Sizes of 18.1 nm<sup>a</sup>

particle composition	$H_{\text{hf}}$ (kOe)	IS (mm/s)	QS (mm/s)	$\Gamma$ (mm/s)	$S$ (%)
$T = 300 \text{ K}$					
$\text{Fe}_3\text{O}_4$ ( $\text{Fe}^{3+} + \text{Fe}^{2+}$ in B-site)	410(2)	0.595(5)	-0.086(5)	0.78(1)	44.6(5)
$\text{Fe}_3\text{O}_4$ ( $\text{Fe}^{3+}$ in A-site)	440(1)	0.232(5)	0.642(5)	0.77(1)	20.7(8)
$\gamma\text{-Fe}_2\text{O}_3$	459(1)	0.373(5)	-0.142(3)	0.73(3)	34.7(8)
$T = 80 \text{ K}$					
$\text{Fe}_3\text{O}_4$ ( $\text{Fe}^{3+}$ in B+A-sites)	487(2)	0.427(5)	0.102(5)	0.72(3)	35.7(8)
$\text{Fe}_3\text{O}_4$ ( $\text{Fe}^{2+}$ in B-site)	455(2)	0.844(5)	-0.290(5)	0.78(3)	17.6(8)
$\gamma\text{-Fe}_2\text{O}_3$	514(1)	0.504(5)	-0.071(3)	0.67(3)	46.7(8)

<sup>a</sup>  $H_{\text{hf}}$  is the hyperfine magnetic field at  $^{57}\text{Fe}$  nuclei, IS is the isomer shift relative to  $\alpha\text{-Fe}$  at room temperature, QS is the quadrupole shift,  $\Gamma$  is the line width, and  $S$  is the area of the spectrum component.

values of the parameters, two components are attributed to  $\text{Fe}^{3+}$  and  $\text{Fe}^{2+}$  ions in octahedral (B) and tetrahedral (A) sites of magnetite  $\text{Fe}_3\text{O}_4$  (see details in Table 2) and the third component belongs to  $\text{Fe}^{3+}$  ions in maghemite  $\gamma\text{-Fe}_2\text{O}_3$ .<sup>19,20</sup> Assuming the same Mössbauer probability in magnetite and maghemite, we have evaluated from the resonance-line areas  $S$  that the content of  $\text{Fe}_3\text{O}_4$  and  $\gamma\text{-Fe}_2\text{O}_3$  in this compound is in a ratio of about 0.65:0.35. The room-temperature spectrum of magnetite shows that the ratio of the line areas for octahedral B and tetrahedral A sites,  $S_B/S_A$ , is close to 2 (see Table 2) which indicates a stoichiometric composition  $(\text{Fe}^{3+})_{\text{tet}}[\text{Fe}^{2+}\text{Fe}^{3+}]_{\text{oct}}\text{O}_4$  of the magnetite particles. When temperature is changed from 300 to 80 K, the Mössbauer spectra reveal the redistribution of the line intensities in the left-hand part of the spectra, Figure 8, which indicates that the Verwey phase transition occurs in the 18.1-nm-size nanoparticles between these temperatures.<sup>20</sup>

For the particles with smaller sizes, 12.1, 10.6, and 8.8 nm, the room-temperature Mössbauer spectra show very broadened single or doublet lines (see Figure S2 in the Supporting Information) which can be fit to a superposition of a paramagnetic doublet and a magnetic sextet with wide distribution of the hyperfine magnetic field at iron nuclei. Such spectra are typical of superparamagnetic behavior with slow spin relaxation.<sup>19,21,22</sup> At 80 K, the spectra of the particles with all sizes show a well-developed magnetic splitting (see Figure S2 in the Supporting Information) which indicates that even for the smallest particle size ( $d = 8.8 \text{ nm}$ ) the blocking temperature  $T_b$  is well above 80 K. In the particles of 12.1-nm size, the hyperfine parameters (isomer shift IS and magnetic hyperfine field  $H_{\text{hf}}$  values) of the 80- and 300-K-Mössbauer spectra indicate the presence of the  $\text{Fe}^{2+}$  ions, which is connected with the magnetite nanoparticles.<sup>20,23</sup> From the line areas, we evaluated the content of  $\text{Fe}_3\text{O}_4$  and  $\gamma\text{-Fe}_2\text{O}_3$  in the 12.1 nm particles which is in a ratio of about 0.60:0.40. The room-temperature spectra show that the Mössbauer component with higher magnetic field  $H_{\text{hf}}$  has the larger isomer shift value. It means that the blocking temperature for magnetite in these particles is higher than in maghemite. The Mössbauer spectra of the particles with 10.6- and 8.8-nm size can be fit to two components with broad distributions of the hyperfine parameters. However, the isomer shift IS values for both components are typical of  $\text{Fe}^{3+}$  iron ions in oxides.<sup>23</sup> At 80 K, the IS value is 0.45 mm/s, and it reduces to 0.34 mm/s at 300 K due to the second-order Doppler effect.<sup>24</sup> This indicates that only the maghemite  $\gamma\text{-Fe}_2\text{O}_3$  phase exists in the 10.6- and 8.8-nm-size

**Figure 9.** Mössbauer spectra of the monodisperse iron oxide NPs with diameters of 10.6 nm (run 2 in Table 1) obtained at intermediate temperatures between 80 and 300 K. Solid lines are least-squares fits of the experiment to superposition of two components.**Figure 10.** Temperature dependence of the average magnetic hyperfine fields at iron nuclei for two Mössbauer components in the monodisperse NPs of maghemite  $\gamma\text{-Fe}_2\text{O}_3$  with diameters of 10.6 nm. Arrows show the blocking temperatures  $T_{b1}$  and  $T_{b2}$ . Solid lines are guides for eyes.

particles (taking into account that X-ray diffraction shows only the spinel-type crystal structure in these particles).

Figure 9 shows in the Mössbauer spectra of the 10.6-nm-size particles at intermediate temperatures between 80 and 300 K. The spectra indicate that the magnetic ordering is gradually transformed into a paramagnetic state when temperature increases up to 300 K. The broadened spectra lines at intermediate temperatures are due to the slow magnetic relaxation effect which is a typical signature of the superparamagnetic properties of these particles.<sup>19,21</sup> For uniaxial magnetic anisotropy, the process is governed by a spin relaxation time  $\tau = \tau_0 \exp(K_{\text{eff}}V/k_B T)$ , where  $K_{\text{eff}}$  is the magnetic anisotropy constant,  $V$  is the volume of the particle,  $T$  is the temperature,  $k_B$  is Boltzmann's

constant, and  $\tau_0$  is a constant characteristic of the material. In Figure 10, we plot the temperature dependence of the average magnetic hyperfine fields  $H_{\text{hf}}$  at iron nuclei for two Mössbauer components in the spectra of the 10.6-nm-size particles. We have found that at a certain temperature the value of the field starts to decrease very rapidly, and this temperature can be accepted as a blocking temperature  $T_b$ . It is very interesting that the two Mössbauer components exhibit different values of the blocking temperatures  $T_{b1} = 150$  K and  $T_{b2} = 220$  K.

In general, the Mössbauer blocking temperature can vary due to variations in particle size, composition, and surface characteristics of the particles.<sup>25,26</sup> Taking into account that these particles are monodisperse and single-phase, it is reasonable to conclude that these two components are originated from core and shell parts of the particles, which demonstrate different magnetic behavior. It seems that the higher value of blocking temperature  $T_{b2}$  corresponds to the core part of the particles whereas the lower value  $T_{b1}$  is related to the shell. Then, from the areas of the Mössbauer components, we can obtain the relative volumes of the core  $V_{\text{core}}$  and shell  $V_{\text{shell}}$  parts of the spherical-shaped particles and evaluate the thickness of the shell using the equation:

$$R_{\text{particle}} = r_{\text{core}} \sqrt[3]{\frac{V_{\text{shell}}}{V_{\text{core}}} + 1}$$

where  $R_{\text{particle}}$  is the particle radius and  $r_{\text{core}}$  is the radius of the core part of the particle. For the 10.6-nm-size particles, we have found that the thickness of the particle shell is  $(R_{\text{particle}} - r_{\text{core}}) = 1.3 \pm 0.1$  nm.

## Conclusions

The synthesis of monodisperse magnetic iron oxide nanoparticles from irregular submicrometer hematite particles has been successfully carried out. Conceptually, these experiments have important meaning for the synthesis of monodisperse oxide nanoparticles, because the synthesis can be simply viewed as a controlled dissolution–recrystallization process.

**Acknowledgment.** We thank National Science Council of Taiwan and the Russian Academy of Sciences for financial support.

**Supporting Information Available:** Magnetization curves for 12.1, 14.5, and 22.3 nm NPs, and Mössbauer spectra for 12.1, 10.6, and 8.8 nm NPs. This material is available free of charge via the Internet at <http://pubs.acs.org>.

## References

- (1) (a) Park, J.; Lee, E.; Hwang, N. M.; Kang, M.; Kim, S. C.; Hwang, Y.; Park, J. G.; Hoh, H. J.; Kim, J. Y.; Park, J. H.; Hyeon, T. *Angew. Chem., Int. Ed.* **2005**, *44*, 2872. (b) Rogach, B. A. L.; Talapin, D. V.; Shevchenko, E. V.; Kornowski, A.; Haase, M.; Weller, H. *Adv. Funct. Mater.* **2002**, *12*, 653. (c) Klokkenburg, M.; Erne, B. H.; Meeldijk, J. D.; Wiedenmann, A.; Petukov, A. V.; Dullens, R. P. A.; Philipse, A. P. *Phys. Rev. Lett.* **2006**, *97*, 185702. (d) Alivisatos, A. P. *Science* **1996**, *271*, 933. (e) Lin, C. R.; Chiang, R. K.; Wang, J. S.; Sung, T. W. *J. Appl. Phys.* **2006**, *99*, 1.
- (2) (a) Shevchenko, E. V.; Talapin, D. V.; Kotov, N. A.; O'Brien, S.; Murray, C. B. *Nature* **2006**, *439*, 55. (b) Tang, Z.; Zhang, Z.; Wang, Y.; Glotzer, S. C.; Kotov, N. A. *Science* **2006**, *314*, 174. (c) Yavuz, C. T.; Mayo, J. T.; Yu, W. W.; Prakash, A.; Falkner, J. C.; Yean, S.; Cong, L.; Shipley, H. J.; Kan, A.; Tomson, M.; Natelson, D.; Colvin, V. L. *Science* **2006**, *314*, 964. (d) Giersig, M.; Hilgendorff, M. *Eur. J. Inorg. Chem.* **2005**, 3571. (e) Colfen, H.; Antonietti, M. *Angew. Chem., Int. Ed.* **2005**, *44*, 5576. (f) Zaitseva, N.; Dai, Z. R.; Leon, F. R.; Krol, D. *J. Am. Chem. Soc.* **2005**, *127*, 10221. (g) Niemeyer, C. M. *Angew. Chem., Int. Ed.* **2001**, *40*, 4128.
- (3) (a) Hyeon, Y.; Lee, S. S.; Park, J.; Chung, Y.; Na, H. B. *J. Am. Chem. Soc.* **2001**, *123*, 12798. (b) Woo, K.; Hong, J.; Choi, S.; Lee, H. W.; Ahn, J. P.; Kim, C. S.; Lee, S. W. *Chem. Mater.* **2004**, *16*, 2814. (c) Peng, S.; Wang, C.; Xie, J.; Sun, S. *J. Am. Chem. Soc.* **2006**, *128*, 10676. (d) Lai, J. I.; Shafi, K. V. P.; Ulman, A.; Loos, K.; Lee, Y.; Vogt, T.; Lee, W. L.; Ong, N. P. *J. Phys. Chem. B* **2005**, *109*, 15. (e) Hyeon, T. *Chem. Commun.* **2003**, 8, 927.
- (4) Rockenberger, J.; Alivisatos, A. P. *J. Am. Chem. Soc.* **1999**, *121*, 11595.
- (5) (a) Sun, S.; Zeng, H. *J. Am. Chem. Soc.* **2002**, *124*, 8204. (b) Li, Z.; Chen, H.; Bao, H.; Gao, M. *Chem. Mater.* **2004**, *16*, 1391. (c) Song, Q.; Ding, Y.; Wang, Z. L.; Nhang, Z. J. *J. Phys. Chem. B* **2006**, *110*, 25547. (d) Sun, S.; David, H.; Robinson, D. B.; Raoux, S.; Rice, P. M.; Wang, S. X.; Li, G. *J. Am. Chem. Soc.* **2004**, *126*, 273. (e) Pinna, N.; Grancharov, S.; Beato, P.; Bonville, P.; Antonietti, M.; Niederberger, M. *Chem. Mater.* **2005**, *17*, 3044.
- (6) Redl, F. X.; Black, C. T.; Papaefthymiou, G. C.; Sandstrom, R. L.; Yin, M.; Zeng, H.; Murray, C. B.; O'Brien, S. P. *J. Am. Chem. Soc.* **2004**, *126*, 14583.
- (7) (a) Jana, N. R.; Chen, Y.; Peng, X. *Chem. Mater.* **2004**, *16*, 3931. (b) Park, J.; An, K.; Hwang, Y.; Park, J. G.; Noh, H. J.; Kim, J. Y.; Park, J. H.; Hwang, N. M.; Hyeon, T. *Nat. Mater.* **2004**, *3*, 891. (c) Garuntu, D.; Caruntu, G.; Chen, Y.; O'Connor, C. J.; Goloverda, G.; Kolesnichenko, V. L. *Chem. Mater.* **2004**, *16*, 5527.
- (8) Dumestre, F.; Chaudret, B.; Amiens, C.; Renaud, P.; Fejes, P. *Science* **2004**, *303*, 821.
- (9) Yu, W. W.; Falkner, J. C.; Yavuz, C. T.; Colvin, V. L. *Chem. Commun.* **2004**, 2306.
- (10) (a) Murray, C. B.; Kagan, C. R.; Bawendi, M. G. *Annu. Rev. Mater. Sci.* **2000**, *30*, 545. (b) Donega, C. D. M.; Liljeroth, P.; Vanmaekelbergh, D. *Small* **2005**, *1*, 1152. (c) Murray, C. B.; Noms, D. J.; Bawendi, M. G. *J. Am. Chem. Soc.* **1993**, *115*, 8706.
- (11) Akanni, M. S.; Okoh, E. K.; Burrow, H. D.; Ellis, H. A. *Thermochim. Acta* **1992**, *208*, 1.
- (12) (a) Chen, H. S.; Lo, B.; Hwang, J. Y.; Chang, G. Y.; Chen, C. M.; Tasi, S. J.; Wang, S. J. *J. Phys. Chem. B* **2004**, *108*, 17119. (b) Liu, H.; Owen, J. S.; Alivisatos, A. P. *J. Am. Chem. Soc.* **2007**, *129*, 305. (c) Murphy, J. E.; Beard, M. C.; Norman, A. G.; Aphrenkiel, S. P.; Johnson, J. C.; Yu, P.; Micic, O. I.; Ellingson, R. J.; Nozik, A. J. *J. Am. Chem. Soc.* **2006**, *128*, 3241.
- (13) (a) Golnen, M.; Balkose, D.; Inal, F.; Ulku, S. *Ind. Eng. Chem. Res.* **2005**, *44*, 1627. (b) Barman, S.; Vasudevan, S. *J. Phys. Chem. B* **2006**, *110*, 651.
- (14) (a) Zhong, X.; Knoll, W. *Chem. Commun.* **2005**, 1158. (b) Zhang, Z.; Liu, S.; Chow, S.; Han, M. Y. *Langmuir* **2006**, *22*, 6335.
- (15) (a) Xi, G.; Xiong, K.; Zhao, Q.; Zhang, R.; Zhang, H.; Qian, Y. *Cryst. Growth Des.* **2006**, *6*, 577. (b) Liang, B. X.; Wang, X.; Zhuang, J.; Chen, Y.; Wang, D.; Li, Y. *Adv. Funct. Mater.* **2006**, *16*, 1805. (c) Zhang, D. F.; Sun, L. D.; Yin, J. L.; Yan, C. H.; Wang, R. M. *J. Phys. Chem. B* **2005**, *109*, 8786.
- (16) Sugimoto, T. *Monodispersed Particles*; Elsevier: New York, 2001.
- (17) Yin, Y.; Alivisatos, A. P. *Nature* **2005**, *437*, 664.
- (18) Chen, Y.; Kim, M.; Lian, G.; Johnson, M. B.; Peng, X. *J. Am. Chem. Soc.* **2005**, *127*, 13331.
- (19) Dorman, J. L.; Fiorani, D., Eds. *Magnetic Properties of Fine Particles*; Elsevier: Amsterdam, 1992.
- (20) Van Diepen, A. H. *Physica B* **1977**, *86–88*, 955.
- (21) Kundig, W.; Bommel, H.; Constabaris, G.; Lindquist, R. H. *Phys. Rev.* **1966**, *142*, 327.
- (22) Coey, J. M. D.; Spender, M. D.; Morrish, A. H. *Solid State Commun.* **1970**, *8*, 1605.
- (23) Shenoy, G. K.; Wagner, F. E. *Mössbauer Isomer Shifts*; North Holland: Amsterdam, 1978.
- (24) Greenwood, N. N.; Gibb, T. C. *Mössbauer Spectroscopy*; Chapman and Hall, Ltd.: London, 1978.
- (25) Badker, F.; Hansen, M. F.; Koch, C. B.; Lefmann, K.; Mørup, S. *Phys. Rev.* **2000**, *B61*, 6826.
- (26) Parafthymiou, G. C. *MRS Proc.* **2000**, *395*, C2.4.1.

CG0706013